

# Determining the Proximity Effect Induced Magnetic Moment in Graphene by Polarised Neutron Reflectivity and X-ray Magnetic Circular Dichroism

R. O. M. Aboljadayel,<sup>1,\*</sup> D. M. Love,<sup>1</sup> C. A. F. Vaz,<sup>2</sup> R. S. Weatherup,<sup>3</sup>  
 P. Braeuninger-Weimer,<sup>3</sup> M.-B. Martin,<sup>3</sup> A. Cabrero-Vilatela,<sup>3</sup> A.  
 Ionescu,<sup>1,†</sup> C. J. Kinane,<sup>4</sup> T. R. Charlton,<sup>4</sup> J. Llandro,<sup>1</sup> P. M. S.  
 Monteiro,<sup>1</sup> C. H. W. Barnes,<sup>1</sup> S. Hofmann,<sup>3</sup> and S. Langridge<sup>4</sup>

<sup>1</sup>*Cavendish Laboratory, Physics Department,  
 University of Cambridge, Cambridge CB3 0HE, United Kingdom.*

<sup>2</sup>*Swiss Light Source, Paul Scherrer Institut, 5232 Villigen PSI, Switzerland*

<sup>3</sup>*Department of Engineering, University of Cambridge,  
 Cambridge CB3 0FA, United Kingdom.*

<sup>4</sup>*ISIS Facility, STFC Rutherford Appleton Laboratory,  
 Harwell Science and Innovation Campus,  
 Oxon, OX11 0QX, United Kingdom.*

(Dated: February 28, 2025)

## Abstract

We report the magnitude of the induced magnetic moment in CVD-grown epitaxial and rotated-domain graphene as a result of the proximity effect in the vicinity of the ferromagnetic substrates Co and Ni, using polarised neutron reflectivity (PNR). Although rotated-domain graphene is known to interact weakly with the ferromagnetic underlayer in comparison with the epitaxial graphene, the PNR results indicate an induced magnetic moment of  $\sim 0.57 \mu_B/C$  atom at 10 K for both structures. The origin of the induced magnetic moment is found to be due to the opening of the graphene's Dirac cone as a result of the strong C  $p_z$ - $3d$  hybridisation, which was confirmed by additional PNR measurements using a non-magnetic  $Ni_9Mo_1$  and Cu substrates. We validated our PNR fitting models using the Bayesian uncertainty analysis and corroborated the results by X-ray magnetic circular dichroism measurements.

---

\* roma2@cam.ac.uk

† ai222@cam.ac.uk

## I. INTRODUCTION

Graphene is a promising material for many technological and future spintronic device applications such as spin-filters [1, 2], spin-valves and spin field-effect transistors due to its excellent transport properties [3, 4]. A single layer graphene can have an intrinsic charge carrier mobility of more than 200,000 cm<sup>2</sup>/Vs at room temperature (RT) [5], and a large spin relaxation time as a result of its long electron mean free path and its negligible spin-orbit and hyperfine couplings [2, 6].

Manipulating spins directly in the graphene layer has attracted great attention as it opens new ways for using this 2D material in spintronics applications [2, 7]. This has been realised via various approaches such as through the proximity-induced effect [2, 8–11], chemical doping of the graphene surface [6] or through a chemically-induced sublattice [12]. Here, we report the feasibility of the first method in utilising the exchange coupling of local moments between graphene and a ferromagnetic (FM) material to induce a magnetic moment in graphene.

Graphene is a zero-gap semiconductor because the  $\pi$  and  $\pi^*$  bands meet at the Fermi energy ( $E_F$ ), at the corner of the graphene's Brillouin zone ( $K$  points), i.e. at degenerate points forming the Dirac point ( $E_D$ ), where the electronic structure of these bands can be described using the tight-binding model [13, 14]. However, the adsorption of graphene on a strongly interacting metal distorts its intrinsic band structure around  $E_D$ . This is a result of the overlap of the graphene's valence band with that of the metal substrate due to the break of degeneracy around  $E_D$  in a partially-filled  $d$ -metal [2, 13, 15–17]. Thus, in the proximity of a FM-TM an induced magnetic moment in graphene is expected, as discussed in the *universal model* proposed by Voloshina and Dedkov [18].

It is widely accepted that graphene's C atoms are assembled in what is known as the top-*fcc* configuration on top of close-packed (111) films, where the C atoms are placed on top of the atoms in the first and third layers of the TM substrate [15, 16, 18]. The strength of the graphene-TM interaction is influenced by the lattice mismatch, the graphene-TM bond length and the position of the  $d$  orbital of the TM relative to  $E_F$ . Therefore, Ni(111) and Co(111) substrates were used since they have a small lattice mismatch of -1.2% for Ni(111) and -1.6% for Co(111), a bond length of 2.03 – 2.16 Å and their  $d$  orbitals are positioned  $\sim 1.1 - 1.3$  eV below  $E_F$  (i.e. forming  $\pi$ - $d$  hybrid states around the  $K$  points)

[16–20]. Epitaxial and rotated-domain graphene structures were investigated since rotated graphene is expected to interact more weakly with the TM film underneath due to the loss of epitaxial relationship and a lower charge transfer from the TM due to missing direct  $\text{Ni}_{\text{top}}\text{-C}$  interaction [21]. Therefore, a smaller magnetic moment is expected to be induced in rotated-domain graphene.

We have studied the structural, magnetic and electronic properties of epitaxial- and rotated-domain graphene grown on Ni and Co films, confirmed the presence of magnetic moment in graphene by element-specific XMCD and measured the induced magnetic moment of  $\sim 0.57 \mu_B/\text{C}$  at 10 K for both samples using PNR. We then validated the PNR fitting models and studied the correlation between the fitted parameters using Bayesian uncertainty analysis.

This paper is organised as follows: We first give a description of the sample preparation and their properties in Section II and Section III, and the X-ray magnetic dichroism (XMCD) results are discussed in Section IV. In Section V, we present the polarised neutron reflectivity (PNR) measurements and the Bayesian uncertainty analysis. The additional PNR experiments on graphene/ $\text{Ni}_9\text{Mo}_1$  and graphene/Cu are discussed in Section VI. We also compare our results with those reported in the literature for graphene on Ni and for other carbon-based films on transition-metal (TM) substrates [8, 22, 23].

Although graphene/FM interfaces have been previously investigated using XMCD, no direct quantitative analysis of the induced magnetic moment in graphene was carried out [2, 8]. Therefore, to our knowledge, our attempt is the first reported approach in using PNR and XMCD sum rules to estimate the induced magnetic moment in graphene. This is due to the thinness of graphene which is close to the resolution of the PNR technique, and the difficulty in processing the XMCD C  $K$ -edge signal due to the contribution of the carbon contamination in the beamline optics. We also prove that the measured induced magnetic moment in graphene is due to the hybridisation of the C  $p_z$  orbital with the  $3d$  bands of the TM by carrying out additional PNR measurements on non-magnetic  $\text{Ni}_9\text{Mo}_1(111)$  and polycrystalline Cu substrates.

## II. SAMPLE PREPARATION

The sample preparation procedure involved two stages; the growth of the TM films using magnetron sputtering and the growth of graphene by chemical vapour deposition (CVD).

### A. Growth of the transition metal films

The TM films were deposited at RT on 1 mm thick  $\text{Al}_2\text{O}_3(0001)$  substrates using a CEVP magnetron sputtering chamber with a base pressure of  $1.2 - 2 \times 10^{-8}$  mTorr. The thick substrates were used to reduce the possibility of sample deformation which could affect the reflectivity measurements. The deposition of the TM films was performed using 99.9% pure Ni and Co targets. A DC current of 0.1 A and a constant flow of pure Argon of 14 sccm were used to grow 80 nm of highly textured Ni(111) and Co(111) films at a rate of 0.02 nm/s in a plasma pressure of 2 mTorr.

### B. Growth of graphene by CVD

The samples were then transferred into a CVD system for the growth of graphene directly on Ni(111) and Co(111) films on  $\sim 2 \text{ cm} \times 2 \text{ cm}$  substrates. Growth recipes similar to those reported by Patera *et al.* [21] were adapted to obtain epitaxial and rotated-domain graphene directly on the Ni film. For the Co film, rotated-domain graphene was grown by first introducing  $\text{H}_2$  gas at a rate of 180 sccm to the CVD chamber with a base pressure of  $2.7 \times 10^{-6}$  mbar. Then, the CVD growth chamber was heated to  $630 \text{ }^\circ\text{C}$  for 12 minutes and the sample was then exposed to  $\text{C}_2\text{H}_4$  with a flow rate of 0.63 sccm for 60 minutes before it was cooled down to RT in vacuum. This approach reduces any oxidised TM back to clean Ni or Co film before the growth of graphene.

The SEM images shown in Figure 1 illustrate the structure of epitaxial and rotated graphene on Ni and Co with a surface coverage of  $\sim 70\% - 90\%$ . Figure 1 (a) shows a homogenous monolayer of graphene on Ni, whereas the darker grey regions in Figure 1 (b) are the differently oriented graphene domains. However, Figure 1 (c) shows different shades of grey suggesting mixed areas of single, bi- and few-layer graphene grown on Co. The low-energy electron diffraction (LEED) in Figure 1 (d) shows the graphene's hexagonal pattern epitaxially grown on the Ni(111) substrate. The  $(1 \times 1)$  grown graphene structure

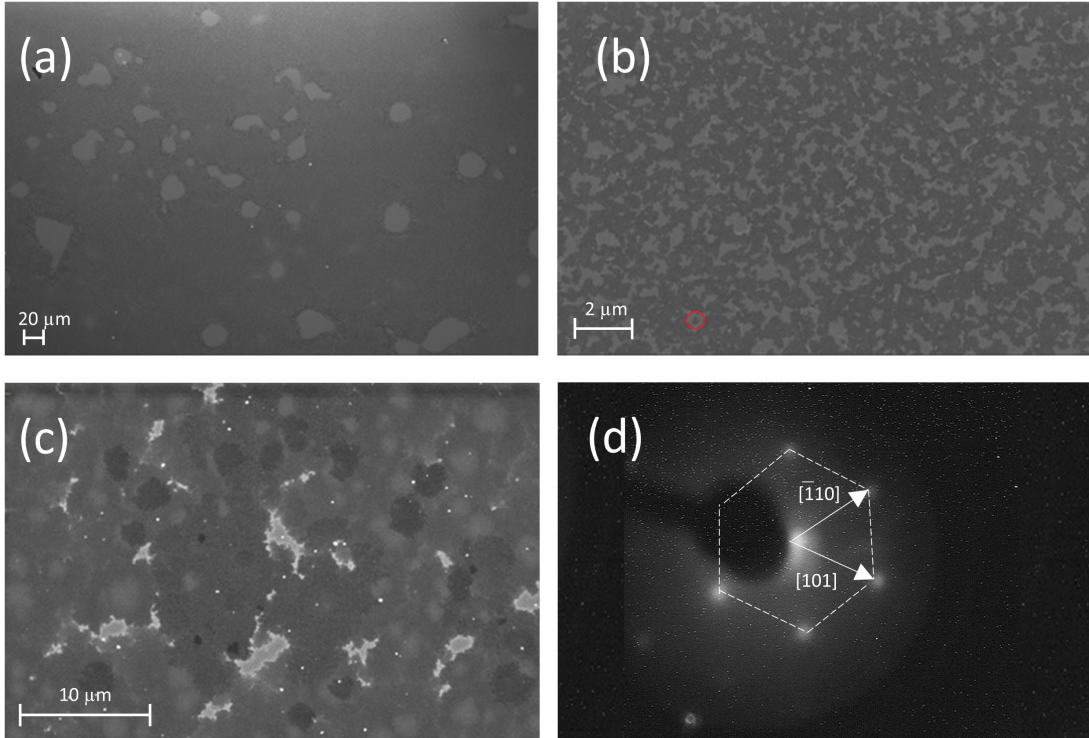


FIG. 1. SEM images at 1 kV showing the graphene domains for (a) epitaxial graphene/Ni and (b) rotated graphene/Ni and at 2 kV for (c) rotated graphene/Co. (d) The LEED diffraction pattern of epitaxial graphene on a Ni(111) substrate at 300 eV. The red circle in (b) highlights a single graphene domain with a diameter of  $\sim 0.25 \mu\text{m}$ .

is confirmed since no additional diffraction spots are observed in the LEED pattern.

### III. RAMAN MEASUREMENTS

The quality, number of graphene layers, the doping and defect density in the grown graphene samples were investigated using Raman spectroscopy with a 532 nm excitation laser wavelength ( $50\times$  objective lens and  $\sim 1 \mu\text{m}$  laser spot size). Graphene has two main characteristic peaks in the Raman spectra, a first-order Raman scattering (RS)  $G$  peak at  $\sim 1582 \text{ cm}^{-1}$ , corresponding to a single phonon excitation in the first Brillouin zone (BZ), located at the frequency of the in-plane longitudinal optical ( $LO$ ) and transverse optical ( $TO$ ) phonon branches at the  $\Gamma$  point [24, 25]; and a second-order (double-resonance) RS  $2D$  peak at  $\sim 2700 \text{ cm}^{-1}$  in which two phonons are excited in the scattering process. The

RS for the  $2D$  line is known as an inter-valley process and is usually used as an indication of a perfect crystalline honeycomb-like structure [25, 26]. On the other hand, the  $G$  peak is a graphite-like line which can be observed in different carbon-based materials [26]. Graphene also possesses other second-order RS peaks such as  $D+D''$  located at  $\sim 2450 \text{ cm}^{-1}$  and  $2D'$  at  $\sim 3200 \text{ cm}^{-1}$  and disorder-induced peaks such as  $D$  at  $\sim 1350 \text{ cm}^{-1}$  and  $D'$  at  $\sim 1600 \text{ cm}^{-1}$  [25, 27].

For the Raman measurements, the graphene was first transferred by a chemical etching process from the metallic films onto a Si substrate with a 300 nm thermally oxidised  $\text{SiO}_2$  layer similar to that reported in Ref. [28]. This is because closely lattice-matched films lead to a loss in the resonance conditions for observing Raman spectra as a result of the strong chemical interaction between the graphene  $\pi$  orbital and the  $d$ -states of Co and Ni, which also alters the graphene's  $p_z$  orbitals. Furthermore, the increase in the C-C bond length to match the lattice of the FM leads to significant changes in the graphene's phonon spectrum [16, 24]. For the transfer process, the samples were cleaved into  $\sim 5 \text{ mm} \times 5 \text{ mm}$  squares and  $\text{HNO}_3$ , diluted to 10% (for Ni) and 20% (for Co), was used as the chemical reagent to etch the metallic films slowly while preserving the graphene layer.

Single-layer graphene is known to have three characteristic features;  $I_{2D}/I_G$  ratio  $> 2$  and a  $2D$  peak fitted with a single Lorentzian with a full-width at half-maximum (FWHM) less than  $40 \text{ cm}^{-1}$  [29]. Furthermore,  $I_D/I_G$  is usually used as an indicator of defects present in graphene, which increases with the increase of disorder in the graphene structure

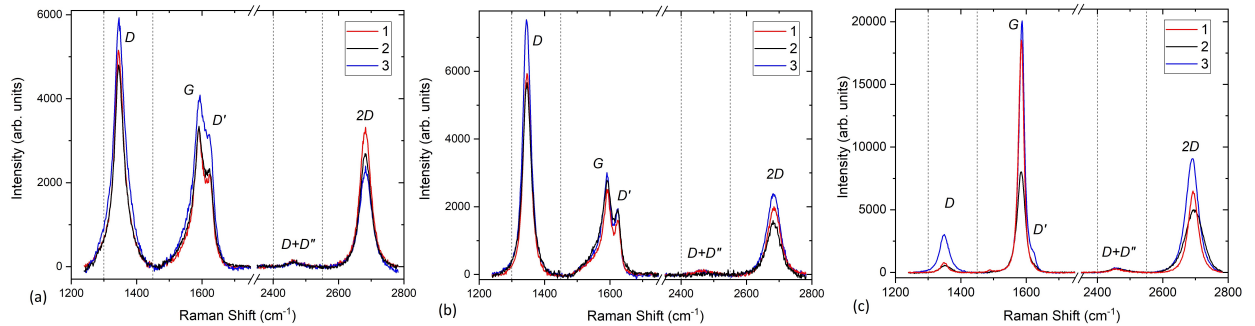


FIG. 2. Room temperature Raman spectroscopy measurements taken after transferring the graphene from (a) the epitaxial Ni, (b) rotated Ni, and (c) rotated Co samples to a Si/ $\text{SiO}_2$  wafer, showing the graphene's characteristic peaks. The dashed vertical lines separate the regions of the different peaks.

[26, 29]. Therefore, good-quality graphene possesses a small  $I_D/I_G$  ratio. Also, the  $D$  peak was reported to change in shape, position and width by increasing the number of graphene layers, while the  $G$  peak is downshifted with increasing the number of graphene layers, but upshifted with increasing the doping level [25]. Moreover, the width of the  $2D$  peak increases with the number of graphene layers [27, 30–32]. Therefore, we assess the quality of our transferred graphene based on these features.

RT Raman scans were taken at three different regions of each sample where all spectra possess the  $D$ ,  $G$ ,  $D'$ ,  $D+D''$  and  $2D$  peaks as shown in Figure 2. The variation in the spectra suggests spatial inhomogeneities in our samples. However, this could also be a result of the chemical etching and transfer process. Although all the  $2D$  peaks shown in Figure 2 were fitted with single Lorentzians, they have relatively broad FWHM. The wide width of the FWHM could be attributed to a high defect density, or to doping from the  $\text{HNO}_3$  used to etch the metallic films. The average FWHM of the  $2D$  peak of epitaxial graphene transferred from the Ni film is  $40.81 \text{ cm}^{-1}$ . However, the high  $D'$  peak shown in Figure 2 (a) indicates a highly defective graphene structure, which is also confirmed by the high  $I_D/I_G$  ratio (average of 1.49). Hence, it is difficult to estimate the number of graphene layers based on the position of the  $G$  and  $2D$  peaks and  $I_{2D}/I_G$  ratio. However, the SEM scan and LEED diffraction pattern in Figure 1 (a) and (d), respectively, show a single epitaxial graphene layer grown on Ni(111). For the rotated domain graphene transferred from the Ni(111) surface (Figure 2 (b)), the average FWHM of the  $2D$  peak ( $46.17 \text{ cm}^{-1}$ ) and the high average  $I_D/I_G$  ratio (2.35) suggest the formation of massively defective or turbostratic (multilayer graphene with relative rotation between the layers) graphene as a result of the occasional overlap of the graphene domains [29].

The Raman spectra of the graphene deposited on Co are shown in Figure 2 (c). The average FWHM of the  $2D$  peak for spectrum 1 and 2 is  $40.11 \text{ cm}^{-1}$ , whereas the FWHM for spectrum 3 is  $63.19 \text{ cm}^{-1}$  which confirm the spatial inhomogeneity seen in the SEM scan (Figure 1 (c)). The average  $I_{2D}/I_G$  ratio of 0.47 (i.e.  $< 1.5$ ) and the  $2D$  peaks with FWHM  $\sim 50 \text{ cm}^{-1}$  suggest a few-layer graphene system [29]. However, the very low average  $I_D/I_G$  ratio (0.09) and the fact that only the blue spectrum (number 3) has a small  $D'$  shoulder suggest that good-quality few-layer graphene with low defect density was grown on the Co film.

Although a few-layer graphene system was grown on Co, we can infer that there are less

than five layers in total since it was reported that only the Raman spectrum of graphene with up to five layers could be distinguished from that of graphite [32]. Furthermore, our results show a higher disorder level in the graphene transferred from the Ni films compared to that transferred from Co which agree with Patera *et al.*, where many defects, associated with Ni, were found trapped in the graphene lattice [21]. A full list of the peak positions and the 2D average FWHM of all the measured samples is provided in the supplemental materials.

#### IV. X-RAY MAGNETIC CIRCULAR DICHROISM (XMCD)

We carried out element selective XMCD measurements to detect and distinguish the magnetisation in the graphene from that of the FM layer. The XMCD experiments were performed at 300 K at the SIM-end station at PSI using total electron yield (TEY) detection mode with 100% circularly polarised light. The rotated-domain graphene samples were set to an incident angle of 30° from the incoming X-ray beam. An electromagnet was fixed at 40° to the incoming X-ray beam and a magnetic field of 0.11 T was applied for 30 seconds in-plane to the surface of the samples to align the film magnetisation along the beam direction. It was then reduced to 0.085 T during the X-ray absorption spectroscopy (XAS) and XMCD measurements. The intensity of the incident X-ray beam was measured with a clean, carbon free, gold mesh placed just before the sample position. This is particularly important for normalising the signal at the C *K*-edge due to the presence of carbon on the surface of the X-ray optical components. Here,

$$\mu_{\text{XAS}} = \frac{1}{2}(\mu_+ + \mu_-), \quad (1)$$

and

$$\mu_{\text{XMCD}} = \mu_+ - \mu_-, \quad (2)$$

where  $\mu_+$  and  $\mu_-$  are the absorption coefficients parallel and antiparallel to the light propagation vector, respectively, normalised to a common value [33].

According to the sum rules, XAS and XMCD spectra can be used to determine the 3*d* orbital angular momentum  $\langle L_z \rangle$  and the spin angular momentum  $\langle S_z \rangle$  for the *L*-edge

using the following expressions [34, 35]:

$$\langle L_z \rangle = -2n_h \cdot \frac{\int_{L_3+L_2} (\mu_+ - \mu_-) dE}{\int_{L_3+L_2} (\mu_+ + \mu_- + \mu_{XAS}) dE}, \quad (3)$$

$$\langle S_z \rangle = -\frac{3}{2}n_h \cdot \frac{\int_{L_3} (\mu_+ - \mu_-) dE - 2 \int_{L_2} (\mu_+ - \mu_-) dE}{\int_{L_3+L_2} (\mu_+ + \mu_- + \mu_{XAS}) dE} \left( 1 + \frac{7 \langle T_z \rangle}{2 \langle S_z \rangle} \right). \quad (4)$$

Here,  $n_h = (10 - n_d)$  is the number of holes in the  $3d$  states, whereas  $n_d$  is the electron occupation number of the  $3d$  states.  $L_3 + L_2$  represent the integration range over the  $L_3$  and  $L_2$  edges and  $\langle T_z \rangle$ , which is the expectation value of the magnetic dipole operator, is known to be very small in TMs and hence it was ignored [36].

In (2),  $\mu_{XMCD}$  is corrected for the light degree of polarisation,  $P$ , and the light's incident angle,  $\theta$ . Therefore, it was multiplied by a factor  $\frac{1}{P \cos \theta}$  [37], where  $\theta$  is measured with respect to the sample's surface, while  $\mu_{XAS}$  remains unchanged [38].

By correcting  $\mu_{XMCD}$  for  $P$  and  $\theta$ , and substituting (2) and (1) into (3) and (4) with  $A$  and  $B$  being the first and second integrals in the numerator, respectively, and  $3C$  as the denominator,  $\langle L_z \rangle$  and  $\langle S_z \rangle$  can be re-written as [34]:

$$\langle L_z \rangle = -\frac{2}{3} \frac{n_h}{P \cos \theta} \left( \frac{A + B}{C} \right) \quad (5)$$

and

$$\langle S_z \rangle = -\frac{n_h}{P \cos \theta} \left( \frac{A - 2B}{2C} \right). \quad (6)$$

The orbital magnetic moment,  $m_o$ , is equal to  $\langle L_z \rangle$ , whereas the spin magnetic moment,  $m_s$ , is given by  $m_s = 2 \langle S_z \rangle$  [35]. Therefore, the total magnetic moment ( $m_{total}$ ) of the sample can be estimated as  $m_{total} = m_o + m_s$  [35, 39, 40]:

In contrast, since the XMCD at the  $K$ -edge measures the transitions from a non-spin-split  $s$  orbital to  $p$  orbital, only  $m_o$  can be obtained [41]:

$$m_o = \frac{n_h}{P \cos \theta} \frac{\int_K \mu_{XMCD}}{\int_K \mu_{XAS}}, \quad (7)$$

For the  $K$ -edge,  $n_h$  becomes equal to  $6 - n_p$ , where  $n_p$  is the electron occupation number in the  $2p$  bands [42]. Since  $m_s = 2m_o/(g - 2)$ , where  $g$  is the gyromagnetic factor [43],  $m_{total}$  can be estimated for the  $K$ -edge.

Figure 3 shows the XAS and XMCD spectra at 300 K for the graphene/Co sample measured at the Co  $L_{2,3}$ -edge and C  $K$ -edge. The Co spectra show no sign of oxidation

and this proves that graphene acts as a good passivation layer against oxidation [44, 45]. The region between the  $L_3$  and  $L_2$  with a constant negative intensity is known as the diffuse magnetism region,  $\mu_{\text{diff}}$ , and it has been observed and reported for Co, Ni and Fe XMCD spectra [33, 46].  $\mu_{\text{diff}}$  is expected to arise as a result of the opposite spin directions for the  $4s$  and  $3d$  electrons, interstitial and  $sp$ -projected magnetic moments, and the fact that it couples antiferromagnetically to the sample's total magnetic moment in  $3d$  elements, except for Mn [33]. Although  $\mu_{\text{diff}}$  has been reported to contribute to about  $-4\%$  and  $-7\%$  to the total magnetic moment in Co and Ni, respectively [33, 47], since the sum rule does not account for  $\mu_{\text{diff}}$ , the integration range over the  $L_3$  was stopped just before  $\mu_{\text{diff}}$  for the calculation of  $m_o$  and  $m_s$  (858.7 eV for the Ni sample and 787.2 eV for Co). On the other hand, the main  $L_3$  peak and the shoulder,  $\mu_{\text{shoulder}}$ , are due to multiple initial-states configuration,  $3d^8$  and  $3d^9$ , respectively, and therefore they were accounted for in the sum rule calculations [33].

The calculated  $\langle L_z \rangle$  and  $\langle S_z \rangle$  of the Co layer obtained by using (5) and (6) are  $0.057 \mu_B$  and  $0.21 \mu_B$ , respectively. Therefore, the total magnetic moment is  $m_{\text{total}} = 0.48 \mu_B / \text{Co atom}$ , which is lower than the previously reported values of  $\sim 1.6 \mu_B$  for bulk Co [35, 48]. The reduced calculated values are attributed to the fact that the Co magnetisation could not be saturated with the applied field of 0.11 T, as confirmed by the SQUID magnetometry measurements shown in Figure 4 (a), taken with the magnetic field applied in-plane ( $0^\circ$ ) and out-of-plane ( $90^\circ$ ) to the sample. The shape of the hystereses and the size of the coercivities of both measurements show that the easy axis is in-plane, whereas the reduced sample moments measured by the SQUID may be due to the error arising from measuring the sample's dimensions accurately. However, the measurements prove that the magnetic field of 0.11 T applied at the start of the XMCD experiments was insufficient to saturate or to prevent the strong demagnetisation of the Co film as can be seen from Figure 4 (c).

We can obtain an upper limit to the orbital moment of the graphene layer by integrating the modulus of the dichroic signal,  $|\mu_{\text{XMCD}}|$ , which is shown in Figure 3 (c), red curve. Even though the dichroic contrast and thus the magnetic moment for the Co film are significantly reduced, the XMCD signal of the C  $K$ -edge (Figure 3 (c)) gives a clear indication that a magnetic moment has been induced in the graphene. Furthermore, although the magnetic dichroism response is expected mainly at the peak corresponding to the  $1s \rightarrow \pi^*$  transition as a result of the C  $p_z$  - Co  $3d$  hybridisation [8], a small magnetic signal is observed at the

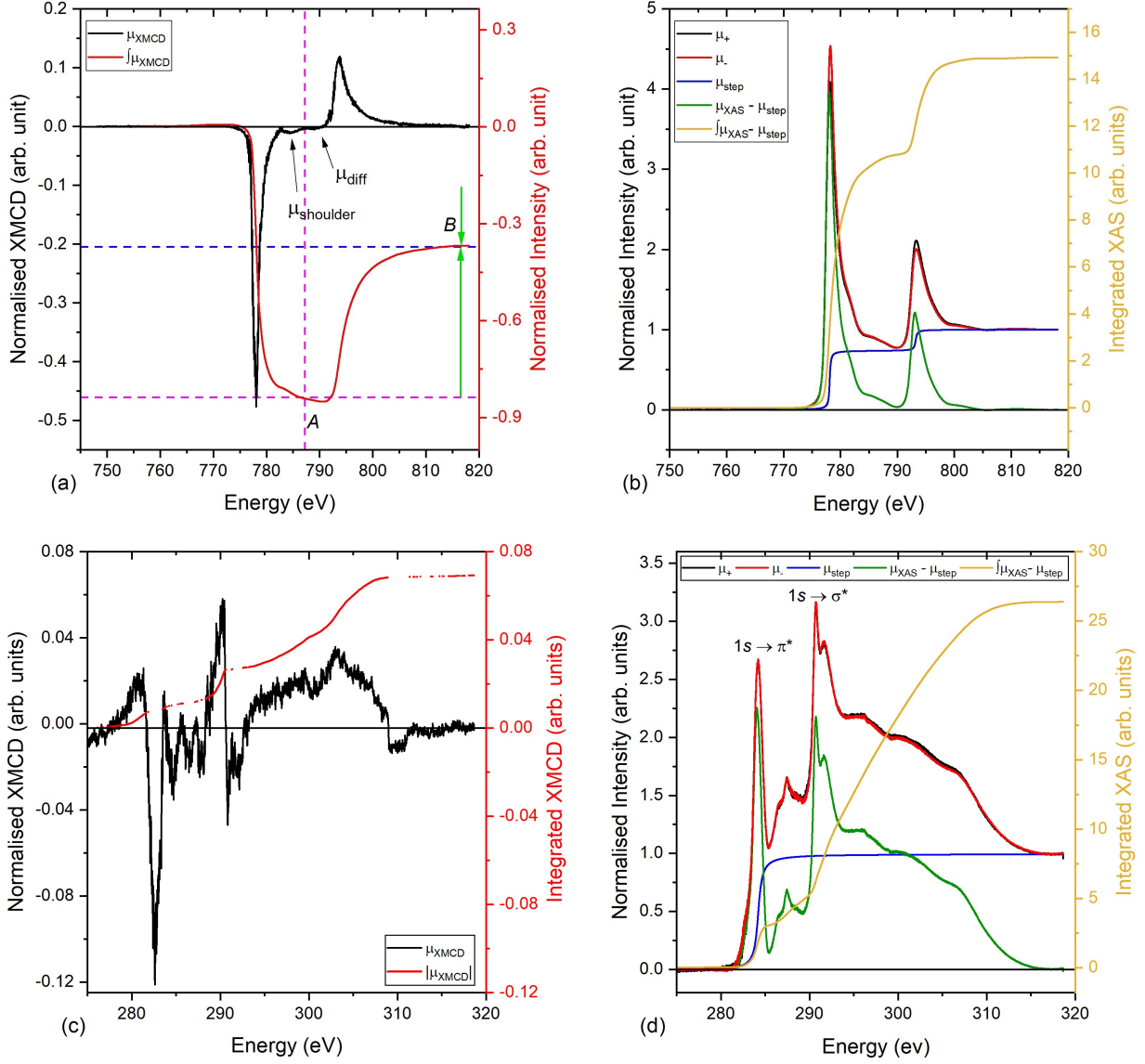


FIG. 3. Absorption spectra for circular polarised light and the areas used to apply the sum rules for the graphene/Co sample measured at 300 K: (a) and (b) XMCD and XAS spectra for Co  $L_{2,3}$ -edge. (c) and (d) XMCD and XAS spectra for the graphene layer.

$1s \rightarrow \sigma^*$  transition peak as well.

The  $m_o$  value was estimated to be  $0.012 \mu_B/\text{C atom}$  for the C  $K$ -edge using  $n_h = 4$ .  $m_s$  is then calculated to be  $0.08 \mu_B/\text{C atom}$ , using  $g = 2.3$ , which is the value reported for graphene grown on SiC [49]. Therefore,  $m_{\text{total}}$  of the graphene grown on Co is  $0.092 \mu_B/\text{C atom}$ . If one corrects for the partial saturation of the Co magnetisation, one obtains an upper value for the graphene magnetic moment  $\mu_{\text{total}} = 0.092 \times \frac{1.6}{0.48} = 0.3 \mu_B/\text{C atom}$ .

Higher sources of errors are expected in the XMCD estimation attributed to the difficulty of applying the sum rules to the C  $K$ -edge spectra in comparison with that for Co and Ni  $L_{2,3}$ -edge. For instance, various studies have been reported for Co and Ni [8, 15, 35, 47, 48, 50–53] which can be used as references for our measurements, but the application of the sum rules has not been reported for graphene before. Also,  $n_h$  has not been measured for C previously. Moreover, the  $g$ -value of the graphene was found to be different depending on the underlying substrate [49, 54, 55], but it has not been reported for graphene on Ni nor on Co substrates. It is also noteworthy to mention the difficulty associated with measuring the C  $K$ -edge due to the C contamination of the optical elements which appear as a significant reduction in the incoming intensity at this particular energy.

The  $\mu_{\text{XMCD}}$  and  $\mu_{\text{XAS}}$  of the Ni  $L_{2,3}$ -edge in the rotated graphene/Ni sample and its corresponding graphene top layer are shown in Figure 5. It is clear from the XMCD spectrum that  $\mu_{\text{shoulder}}$  is more pronounced in Ni than in Co due to the extra electrons in the  $d$  band. Furthermore, although the non-resonant contribution was subtracted from the  $\mu_+$  and  $\mu_-$  spectra, a higher background is measured at the post-edge ( $E > 880$  eV). This tail has been excluded from the sum rules as it is considered part of the non-resonant contribution. The calculated  $m_o$  and  $m_s$  are  $0.084 \mu_B/\text{Ni atom}$  and  $0.625 \mu_B/\text{Ni atom}$ , respectively, and thus  $m_{\text{total}}$  is  $0.709 \mu_B/\text{Ni atom}$ . Considering the 20% accuracy of the XMCD technique in estimating the magnetic moments of materials, the results obtained for Ni is consistent

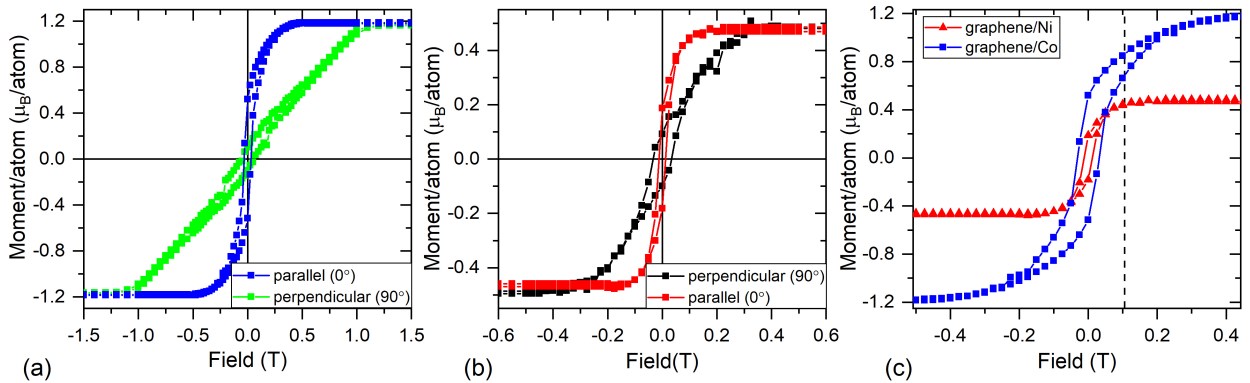


FIG. 4. SQUID measurements showing the hysteresis loops obtained with the field applied parallel ( $0^\circ$ ) and out-of-plane ( $90^\circ$ ) to (a) graphene/Co and (b) graphene/Ni samples. (c) Zoom-in view of the 300 K SQUID measurements where the field is applied parallel to the surface of the graphene/Ni and graphene/Co samples. The dotted vertical line marks the position of 0.11 T.

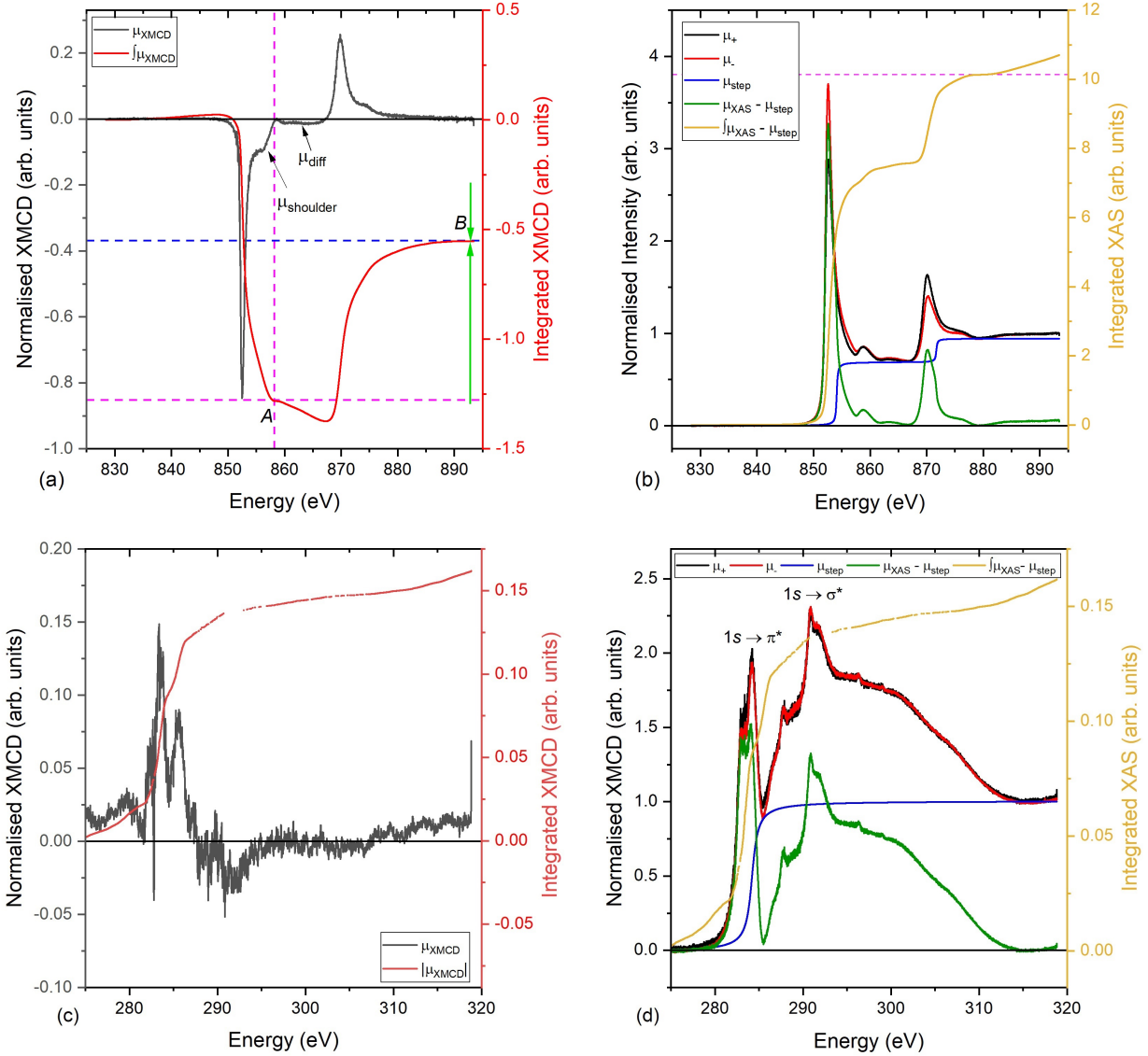


FIG. 5. Absorption spectra for circular polarised light and the areas used to apply the sum rules for the rotated graphene/Ni sample measured at 300 K: (a) and (b) XMCD and XAS spectra for Ni  $L_{2,3}$ -edge. (c) and (d) XMCD and XAS spectra for the graphene layer.

with the values reported in the literature [48]. The slight reduction in the magnetic moment detected by the SQUID (Figure 4 (b)) could be attributed to the same reasons discussed above for the graphene/Co sample.

The C  $K$ -edge spectra for the graphene/Ni sample are shown in Figure 5 (c) and (d). The calculated  $m_o$  for graphene is  $0.034 \mu_B/\text{C atom}$  using  $n_h = 4$ . Therefore,  $m_{\text{total}}$  for the graphene grown on Ni is estimated to be  $0.227 \mu_B/\text{C atom}$ .

Despite the large uncertainties expected for the estimated graphene moments, the XMCD results demonstrate the presence of magnetic polarisation in graphene. For more precise estimates, we turn to PNR.

## V. POLARISED NEUTRON REFLECTIVITY AND THE BAYESIAN UNCERTAINTY ANALYSIS

PNR experiments were carried out to measure the magnetic properties of each layer of the samples individually and to determine the value of the induced magnetic moment in graphene quantitatively. The measurements were conducted at 10 K and under an applied magnetic field of 0.5 T, using the Polref instrument at ISIS (UK), while the fitting of the data was done using GenX [56]. Although both Ni and Co are ferromagnetic at RT, the 10 K measurements are expected to provide a better estimation of the induced magnetic moment due to the lower thermal excitations of the electron spin at low temperature.

The results for the PNR measurements, the corresponding scattering length density (SLD) profiles and the spin asymmetry ( $SA = [R_+ - R_-]/[R_+ + R_-]$ , where  $R_+$  and  $R_-$  are the spin-up and spin-down neutron specular reflectivity, respectively) are shown in Figure 6 for the epitaxial graphene/Ni, rotated graphene/Ni and rotated graphene/Co. The results of the fits to the PNR data are summarised in Table I. For epitaxial and rotated-domain graphene grown on Ni, the PNR fits indicate a slightly thicker epitaxial graphene with a higher error compared to the rotated-domain graphene, which reflects the low relative accuracy of the graphene's thickness estimation expected from a reflectivity technique. However, the results show that the graphene thickness has only a subtle, if any, influence on the amount of the induced magnetisation as can be deduced from the values of the measured magnetic moments listed in Table I.

The fitting procedure was started by pinning the thickness ( $d$ ), roughness ( $\sigma$ ) and density ( $\rho$ ) of the layers to the values obtained from XRR measurements (data not shown) while fitting the remaining parameters: magnetic moment, instrument resolution, background and the incident intensity ( $I_0$ ). The XRR fitted parameters were then allowed to vary within restricted limits as they tend to drift to unrealistic values if no boundaries are set. All the variables were regularly reset to ensure that the fitting routine converged to the same results. Furthermore, fixing the magnetic moment of graphene to zero yielded unrealistic values for

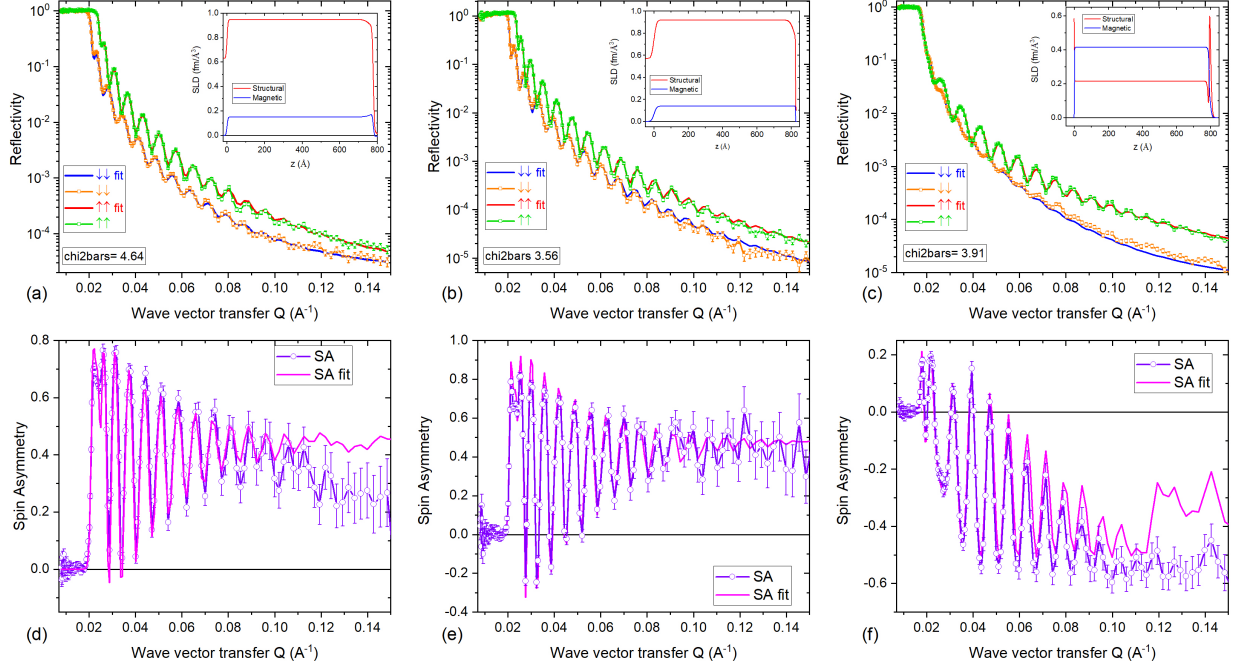


FIG. 6. PNR data (open symbol and line) and fits (solid line), the corresponding SLD profile (insets) and the spin asymmetry for the epitaxial graphene/Ni (a,d), rotated graphene/Ni (b,e) and rotated graphene/Co (c,f), measured at 10 K and with an in-plane magnetic field of 0.5 T.

the thickness and roughness of the graphene layer (which does not agree with the SEM and Raman scans) and poorer fits, especially in the low- and mid- $Q$  range ( $\sim 0.025 - 0.080 \text{ \AA}^{-1}$ ), as shown in Figure 7 for the epitaxial graphene/Ni sample. This agrees with the XMCD results and confirm the consistency of the PNR fits shown in Figure 6 which indicate an induced magnetic moment in the graphene layer.

Additional scenarios were also tested. For example, the oxidation of the TM layer and

TABLE I. Summary of the PNR results.

Sample	FM Layer		Graphene	
	Thickness (nm)	Magnetic Moment ( $\mu_B/\text{atom}$ )	Thickness (nm)	Magnetic Moment ( $\mu_B/\text{atom}$ )
Epitaxial Ni(111)	$77.60 \pm 0.25$	$0.62 \pm 0.02$	$0.31 \pm 0.05$	$0.59 \pm 0.07$
Rotated Ni(111)	$82.3 \pm 0.30$	$0.59 \pm 0.01$	$0.33 \pm 0.20$	$0.57 \pm 0.06$
Rotated Co(111)	$79.9 \pm 0.29$	$1.56 \pm 0.01$	$1.12 \pm 0.18$	$0.58 \pm 0.04$

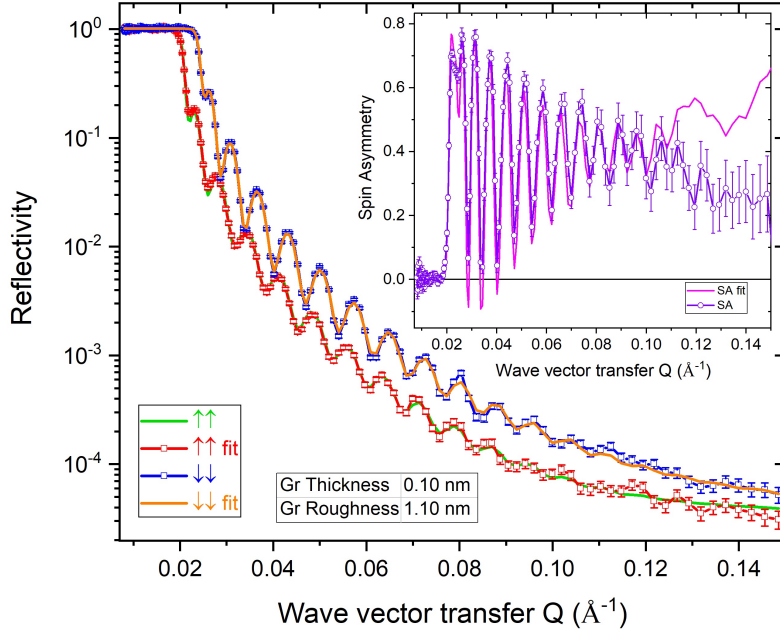


FIG. 7. The PNR data (open symbol and line), fits (solid line) and the spin asymmetry (inset) for the epitaxial graphene/Ni obtained by pinning the magnetic moment in graphene to zero. The inset table lists the deduced thickness and roughness for the graphene layer.

the formation of TM-carbide was examined by embedding an intermediate TM-oxide and TM-carbide layer at the interface between the TM and graphene, but this lead to poorer fits (see supplemental materials) and the best results, shown in Figure 6, were achieved using a simple model: Sapphire/a single layer of TM film/graphene.

Although Co has a higher magnetic moment than Ni, the PNR fits indicate that a similar magnetic moment is induced in the graphene whether grown on Co or as rotated and epitaxial graphene on Ni. This can be attributed to the larger lattice mismatch between the graphene and Co than with the Ni surface.

The PNR fits have shown that a magnetic moment of  $\sim 0.57 \mu_B/C$  was induced in the graphene grown on Ni and Co films. These results indicate larger moments than the value previously predicted by Weser *et al.*, who suggested that the induced magnetic moment for a graphene monolayer grown on a Ni(111) film would be between  $0.05 - 0.1 \mu_B/C$  atom [8]. Their assumption was based on comparing the graphene/Ni system with other C/3d TM structures, such as a C/Fe multilayer [22], and carbon nanotubes (CNTs) on a Co film [23], where a magnetic moment of  $0.05 \mu_B$  and  $0.1 \mu_B/C$  atom was estimated, respectively.

In the former study [22], the magnetic moment of a C/Fe multilayer system with 0.55 nm of C was measured. However, the Dirac cone is a characteristic feature in graphene and CNTs. Therefore, we suggest that a different mechanism other than the break of degeneracy around  $E_D$  may have been responsible for the magnetic moment detected in the C layer in Ref. [22], hence, making it difficult to compare graphene-based heterostructures with other C allotropes/TM systems. On the other hand, although Dirac cones exist in CNTs, a direct quantitative analysis of the induced magnetic moment was not possible from the MFM images reported in Ref [23]. In contrast, PNR provides a direct estimation of the induced magnetic moment in graphene.

We performed Bayesian uncertainty analysis of the graphene/Ni PNR measurements using the Refl1D and Bumps software [57, 58]. This was done to test the validity of the fitting models, understand the correlation between the fitted parameters and hence prove the reliability of the PNR results.

The Bayesian analysis shown in Figure 8 were simulated using sapphire/Ni/Ni/graphene model (the addition of the second Ni layer is discussed below). The reflectivity curves presented in Figure 8 (a) were normalised to that of the sapphire substrate, to eliminate the substrate contribution, thus easily highlighting the features associated with the thin films. The residual graph shown in the inset illustrates the difference between the theoretical model and the measured data, where the fits resulted in a small spread of data of  $\pm 0.06$  from the origin. Furthermore, the analysis yielded a similar structural contribution of the SLD to that shown in Figure 6, while suggesting a higher magnetisation in the graphene.

The graph presented in Figure 8 (b) show the correlation between the fitted parameters. To read the graph and understand the relation between two parameters, a line is drawn vertically for the first parameter, while drawing a horizontal one for the second parameter. The shape inside the box at intersection of the two lines indicates the relation between the parameters. The oval rounded shape shows no correlation between the fitted parameters and that both are at the most probable value. The distorted oval shape reflects some kind of correlation between the different fitted parameters. For instance, there is an approximately linear relationship between the density of C and the roughness of the first Ni layer (*Ni1 rhoM*). However, “*C interface M below*” shows a complicated relation to all other fitted parameters likely due to the constraints applied to the fits.

These cross-correlation plots are mainly used to understand whether or not the model used

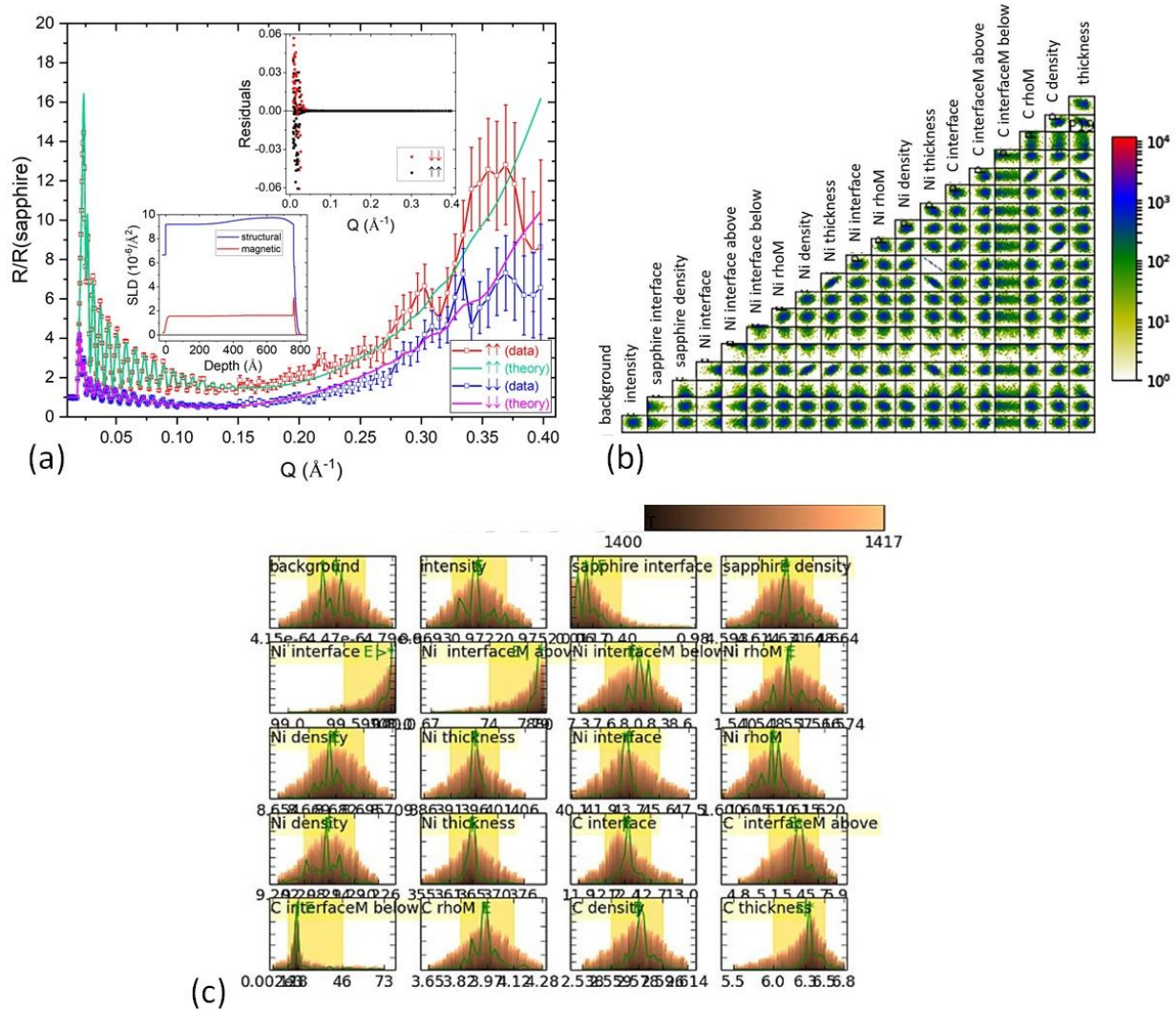


FIG. 8. Bayesian simulations for rotated domains graphene grown on Ni measured at 10 K with an applied of 0.5 T. (a) The PNR reflectivity curves normalised to that of the sapphire substrate. The insets show the corresponding residuals and the resultant SLD profile. (b) The correlation simulation of the fitted parameters. (c) The population histogram and probability distribution of the fitted PNR parameters.

is over-determined i.e., if the number of parameters used is the minimum set of parameters needed to describe the data. Therefore, we are intentionally over-parameterising the Ni layer to obtain the details in the graphene (i.e. whether the effect we are observing is happening in the Ni or the graphene layer). Here, the Ni layer is artificially broken into two layers (Ni1 and Ni2) and the model was run to find the minimum value. This was done to show the strong linear correlation between the thicknesses of the Ni layers. Curiously, we also

observe a weak correlation between *C density* and *Ni2 thickness*. This is likely to be due to the fact that as the carbon density is varied, some of it creates alterations in the SLD profile indistinguishable from the changes of the *Ni2 thickness*.

The population histogram series show the probability distribution for each of the fitted parameters for the rotated Gr/Ni sample at 10 K with an applied field of 0.5 T (Figure 8 (c)). The shaded yellow region represents the 68% confidence interval (one standard deviation around the mean value), while the green line is the highest probability provided that the parameter is fixed at the maximum likelihood value. The histogram and the probability distribution should have a maximum shape for all the parameters of a model to be fully converged, which is the case for our simulation.

## VI. PNR MEASUREMENTS OF THE GRAPHENE/ $\text{Ni}_9\text{Mo}_1(111)$ AND GRAPHENE/Cu SAMPLES

Further PNR experiments were carried out to clarify whether the results are merely due to the C  $p_z$ - $3d$  hybridisation as postulated in Ref. [8, 20] or because of the chemical bonds between the C and TM atoms, as for fullerene/non-magnetic TM as proposed in Ref. [59]. For this purpose, a  $\text{Ni}_9\text{Mo}_1$  film was used with the aim of preserving the *fcc* crystal structure of Ni while suppressing its magnetisation, as suggested in Ref. [60]. Since the Ni is doped by 10% only, the lattice mismatch and bond length to graphene are expected to be similar to that for graphene/Ni(111) sample, but the *d*-orbital position is considerably downshifted with respect to  $E_F$ . See supplemental materials for the sample preparation procedure and its structural properties.

The results of the PNR measurements of the  $\text{Ni}_9\text{Mo}_1$ /graphene sample are shown in Figure 9. A small, but detectable spin splitting and a minute variation in the spin asymmetry are observed. Surprisingly, a higher magnetisation is detected in graphene ( $0.13 \pm 0.08 \mu_B$ ) than in the  $\text{Ni}_9\text{Mo}_1$  film ( $0.08 \pm 0.01 \mu_B$ ), which can be attributed to the small residual moment of the  $\text{Ni}_9\text{Mo}_1$ . Since a small magnetic moment persisted in  $\text{Ni}_9\text{Mo}_1(111)$  at 10 K, the measurements were repeated using a non-magnetic TM, Cu.

As expected, no induced magnetic moment was detected in graphene (results not shown). This is because, firstly, Cu is a non-magnetic TM, and secondly because the weak interaction between the graphene and the Cu surface atoms will not open up the graphene's Dirac cone.

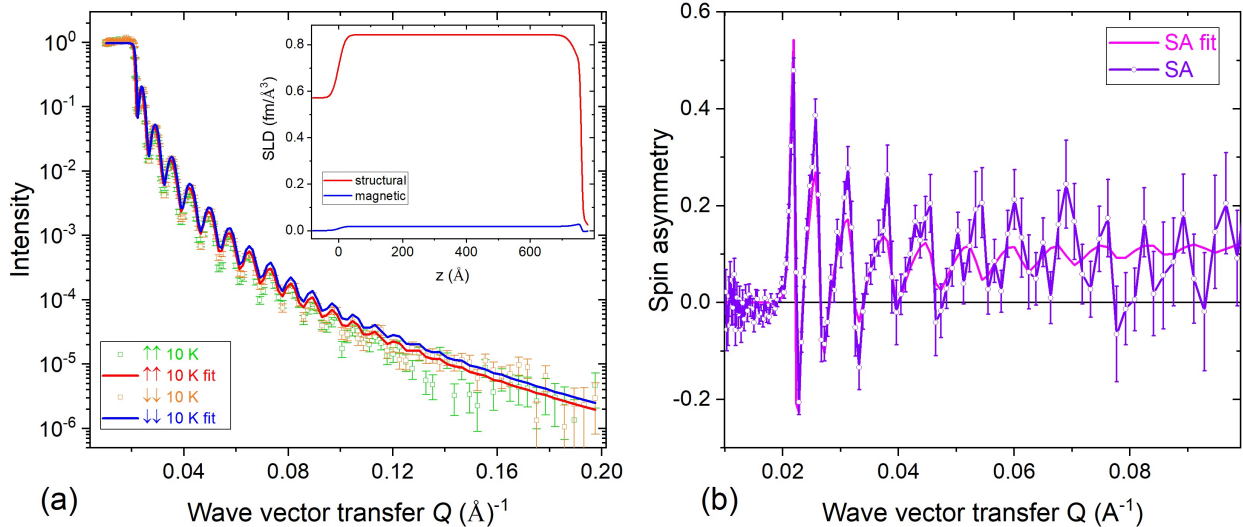


FIG. 9. (a) The PNR data (open symbol and line) and fits (solid line) for the  $\text{Ni}_9\text{Mo}_1/\text{graphene}$  sample and the corresponding SLD (inset). (b) The spin asymmetry of the fit.

Therefore, we conclude that the measured induced magnetic moment in graphene is due to the strong C  $p_z$ -TM  $3d$  hybridisation.

## VII. CONCLUSION

In summary, we have successfully grown graphene by CVD on different TM substrates. Induced magnetic moment in rotated-domain graphene as a result of the proximity effect in the vicinity of a FM substrate was detected by element-specific XMCD measurements at the C  $K$ -edge. PNR experiments were carried out to determine the amount of magnetic moment detected by XMCD. Although a higher magnetic moment was expected to be induced in epitaxial graphene/Ni sample, the PNR results indicate similar magnetic moment of  $\sim 0.57 \mu_B/\text{C}$  atom induced in both structures which is about five times higher than the values predicted in other studies [8, 22, 23]. Furthermore, using Co film, which is a stronger FM but has a larger lattice mismatch with the graphene layer compared to Ni, induced equivalent magnetic moment to that measured in graphene/Ni samples. Additional PNR measurement on non-magnetic Cu film confirms that the induced magnetic moment in graphene arises as a result of the opening of the graphene's Dirac cone due to the strong C  $p_z$ -Ni  $3d$  hybridisation. Therefore, our study is considered the first reported attempt to

estimate the induced magnetisation in graphene by PNR.

## Appendix A: Supplementary Material

### 1. Preparation of the graphene/ $\text{Ni}_9\text{Mo}_1(111)$ sample

A 80 nm thick  $\text{Ni}_9\text{Mo}_1(111)$  film was deposited at RT on a 1 mm thick  $\text{Al}_2\text{O}_3(0001)$  substrate using a CEVP magnetron sputtering from a 99.9% pure  $\text{Ni}_9\text{Mo}_1$  target. A constant DC current of 0.1 A with a constant flow of 14 sccm of pure Argon gas were used to grow the film at a rate of 0.02 nm/s in a plasma of 3 mTorr.

The  $\text{Ni}_9\text{Mo}_1(111)$  film was then transferred into a CVD chamber for the growth of graphene. Pure  $\text{H}_2$  gas was introduced to the CVD at a flow rate of 200 sccm and the sample was then heated to 650 °C, again for 12 minutes before introducing  $\text{C}_2\text{H}_4$  at a rate of 0.24 sccm for 40 minutes and then cooled down to RT to produced rotated-domain graphene on  $\text{Ni}_9\text{Mo}_1(111)$ .

### 2. Preparation of the graphene/Cu sample

The Cu film was deposited on a clean 0.5 mm thick  $\text{Al}_2\text{O}_3(0001)$  substrate using a thermal evaporator with a base pressure of  $3.75 \times 10^{-7}$  mbar. The growth parameters were tuned to evaporate a 950 nm thick film with an evaporation rate of 0.2 nm/s. The growth recipe of graphene on the Cu film is described in Ref. [61].

### 3. Raman Measurements

A transfer method similar to that used for the graphene/Ni and graphene/Co was used for the graphene/ $\text{Ni}_9\text{Mo}_1(111)$  sample before taking the Raman measurements. However, the  $\text{HNO}_3$  was diluted to 5% for  $\text{Ni}_9\text{Mo}_1$ . On the other hand, no transfer procedure was done for the graphene grown on Cu due to the large lattice mismatch between the graphene and Cu ( $\sim 3.5\%$ ) compared to that with Ni and Co [1, 62]. Figure 10 shows the RT Raman spectra for graphene transferred from the  $\text{Ni}_9\text{Mo}_1$  film and for graphene/Cu sample. The average peaks positions and the average 2D FWHM of all the samples are listed in Table II.

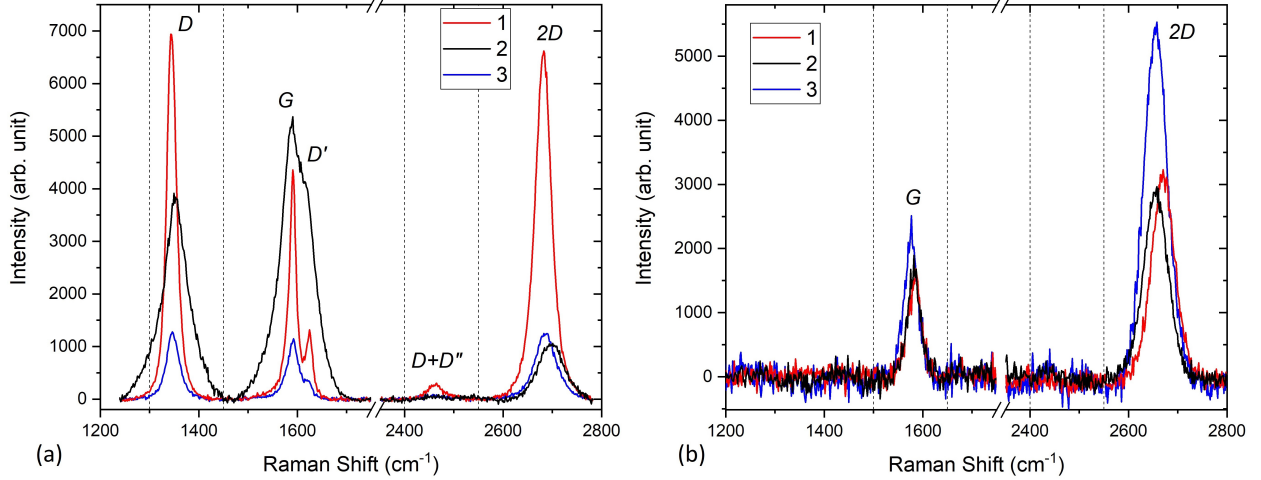


FIG. 10. Room temperature Raman spectroscopy measurements for (a) transferred graphene from the Ni<sub>9</sub>Mo<sub>1</sub>(111) film and (b) graphene/Cu sample, showing the graphene’s characteristic peaks. The dashed vertical lines indicate regions for the different peaks.

Due to the high  $I_{D'}$  of the Raman spectra for the graphene transferred from Ni<sub>9</sub>Mo<sub>1</sub> (Figure 10 (a)), an argument similar to that used for the graphene transferred from Ni(111) can be applied here to explain the spectra. However, the wide spatial variation across the surface of the sample, which could be attributed to formation of occasional strong Mo–C bonding between the graphene and the Ni<sub>9</sub>Mo<sub>1</sub> film, makes it difficult to assess the quality of the graphene grown on Ni<sub>9</sub>Mo<sub>1</sub> based on the 2D FWHM.

Figure 10 (b) shows the two main characteristic peaks of pristine graphene;  $G$  and  $2D$ , while the missing defect induced-peaks from all the three spectra and the  $I_{2D}/I_G$  of about 2 (except for the blue spectrum) reveal that graphene with low defect density was grown on the Cu film. Furthermore, the broad FWHM of the  $2D$  peaks is an indicative of a few-layer graphene as the  $2D$  peak is known to broaden with the number of graphene layers due to the splitting of phonon bands [25]. The noisy spectra is attributed to the background of the coupled polycrystalline Cu substrate [63].

#### 4. PNR Models

Figure 11 to Figure 13 show the PNR fits, their corresponding SLD and spin asymmetry of the various models tested to find the best model for fitting the PNR data for the epitaxial

TABLE II. The results of the Raman measurements summarising the average peaks positions and 2D FWHM for graphene transferred from rotated Co, rotated Ni, epitaxial Ni and Ni<sub>9</sub>Mo<sub>1</sub> and for graphene/Cu sample.

Sample	$D$ (cm <sup>-1</sup> )	$G$ (cm <sup>-1</sup> )	$D'$ (cm <sup>-1</sup> )	$D+D''$ (cm <sup>-1</sup> )	$2D$ (cm <sup>-1</sup> )	$2D$ FWHM (cm <sup>-1</sup> )
Rotated Co	1349.6	1586.9	1621.7	2457.8	2692.3	40.1
Rotated Ni	1346.3	1590.7	1624.8	2464.2	2681.9	46.2
Epitaxial Ni	1344.6	1590.7	1623.1	2462.6	2682.6	40.8
Ni <sub>9</sub> Mo <sub>1</sub>	1346.3	1590.7	1619.9	2464.0	2682.6	39.6
polycrystalline Cu	-	1580.3	-	-	2658.9	47.7

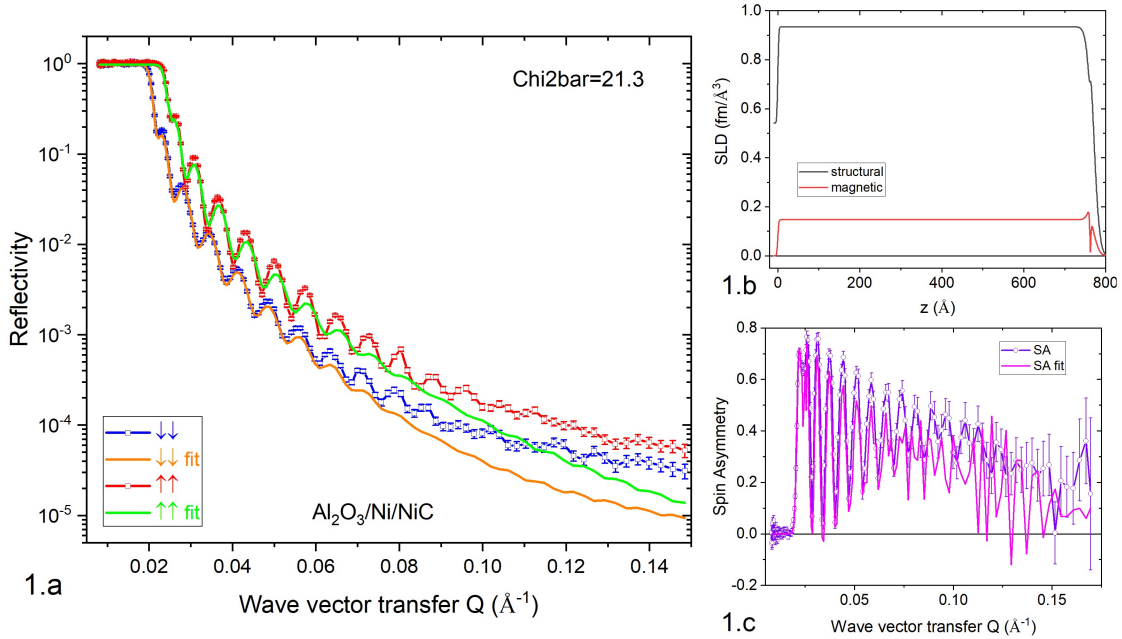


FIG. 11. The PNR data fits, the corresponding SLD profile and spin asymmetry for the epitaxial graphene/Ni(1111) using the model: Al<sub>2</sub>O<sub>3</sub>/Ni/NiC.

graphene/Ni sample. The value of the fit figure of merit ( $\chi^2$ ), and the fitted parameters were used to assess the goodness-of-the fits. For example, Figure 11 shows the results obtained from fitting the data using a model with a NiC at the top layer instead of graphene (i.e. Al<sub>2</sub>O<sub>3</sub>/Ni/NiC). This yielded a poor fit with a  $\chi^2 = 21.3$  and cannot reproduce the reflectivity fringes in the mid- and high-  $Q$  range. It also estimated a reduced number density

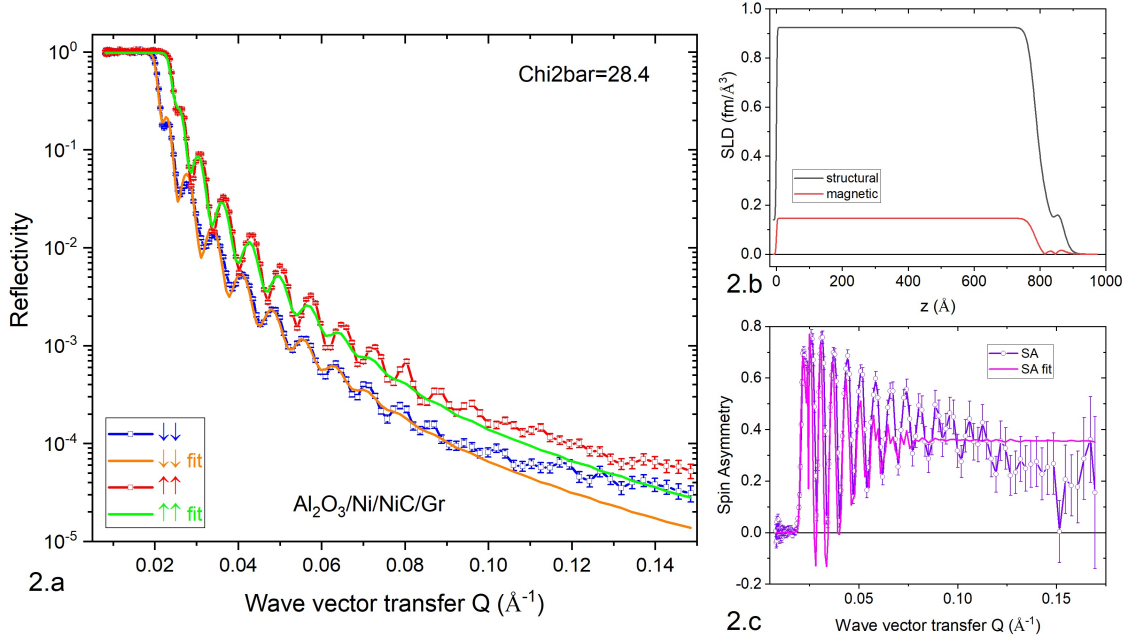


FIG. 12. The 10 K PNR data fits, the corresponding SLD profile and spin asymmetry for the epitaxial graphene/Ni(1111) using the model: Al<sub>2</sub>O<sub>3</sub>/Ni/NiC/Gr.

of  $0.04 \text{ \AA}^3$  for the graphene layer instead of  $0.114 \text{ \AA}^3$ .

In Figure 12, we tested the formation of carbide interdiffusive layer at the interface between the Ni and graphene (i.e Al<sub>2</sub>O<sub>3</sub>/Ni/NiC/Gr). As with the previous model, the simulation does not fit the reflectivity fringes in the mid- and high-  $Q$  ranges. However, although the value estimated with this model for the graphene number density agrees with the literature, it gave unrealistic values for its thickness (0.01 nm, which is the minimum of the fitting range) and roughness (0.25 nm, which is the maximum of the fitting range) and a very high  $\chi^2$  value of 28.4.

Figure 13 shows the results obtained from testing the presence of a NiO layer at the interface between the Ni and graphene. Although this model yielded to a slightly lower  $\chi^2$  compared to the previous model, it estimates a low number density for the graphene similar to model 1. Furthermore, the thickness of the graphene layer deduced from this model is 2 nm (i.e. more than 5 layers of graphene) and this does not agree with the SEM image and Raman scans. Therefore, none of the models shown in this section could fit the PNR data for epitaxial graphene/Ni sample. Similar tests (results not shown) were carried out for the

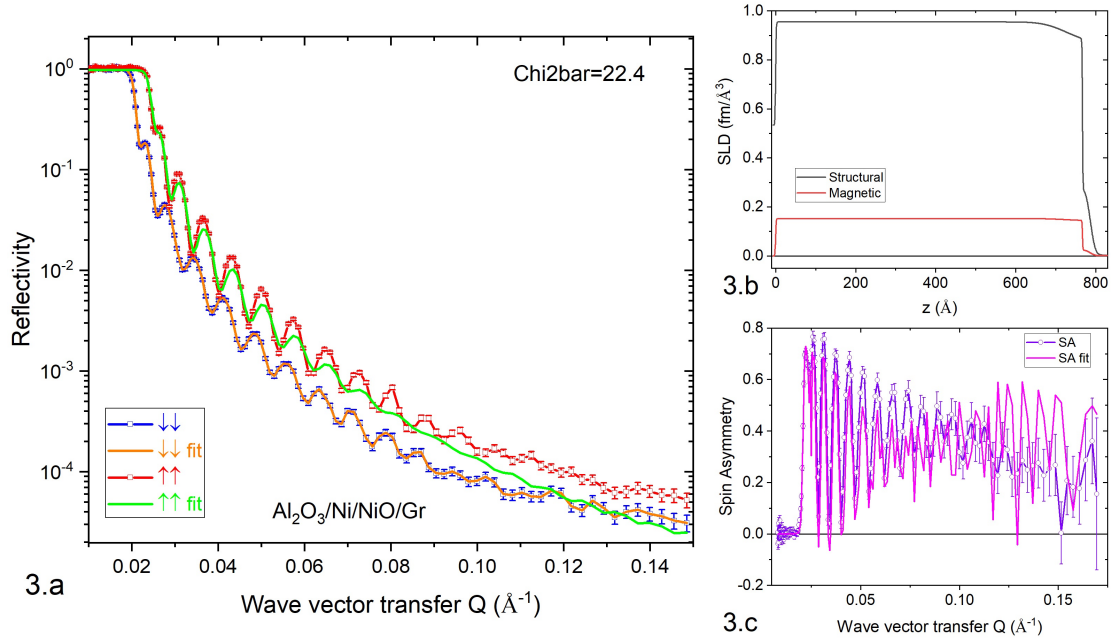


FIG. 13. The 10 K PNR data fits, the corresponding SLD profile and spin asymmetry for the epitaxial graphene/Ni(111) using the model:  $\text{Al}_2\text{O}_3/\text{Ni}/\text{NiO}/\text{Gr}$ .

other samples.

- 
- [1] V. M. Karpan, G. Giovannetti, P. A. Khomyakov, M. Talanana, A. A. Starikov, M. Zwierzycki, J. van den Brink, G. Brocks, and P. J. Kelly, Graphite and Graphene as Perfect Spin Filters, *Physical Review Letters* **99** (2007).
  - [2] M. Weser, E. N. Voloshina, K. Horn, and Y. S. Dedkov, Electronic Structure and Magnetic Properties of the Graphene/Fe/Ni(111) Intercalation-like System, *Physical Chemistry Chemical Physics* **13**, 7534 (2011).
  - [3] E. W. Hill, A. K. Geim, K. Novoselov, F. Schedin, and P. Blake, Graphene Spin Valve Devices, *IEEE Transactions on Magnetics* **42**, 2694 (2006).
  - [4] Y. G. Semenov, K. W. Kim, and J. M. Zavada, Spin Field Effect Transistor with a Graphene Channel, *Applied Physics Letters* **91**, 153105 (2007).
  - [5] S. M. Sze and K. K. Ng, *Physics of Semiconductor Devices* (Wiley, 2006).
  - [6] K. Pi, W. Han, K. M. McCreary, A. G. Swartz, Y. Li, and R. K. Kawakami, Manipulation of Spin Transport in Graphene by Surface Chemical Doping, *Physical Review Letters* **104**,

- 187201 (2010).
- [7] Y. Zhang, X. Sui, D. L. Ma, K. K. Bai, W. Duan, and L. He, Spin-Polarized Semiconducting Band Structure of Monolayer Graphene on Ni (111), *Physical Review Applied* **10**, 1 (2018).
  - [8] M. Weser, Y. Rehder, K. Horn, M. Sicot, M. Fonin, A. B. Preobrajenski, E. N. Voloshina, E. Goering, and Y. S. Dedkov, Induced Magnetism Of Carbon Atoms at the Graphene/Ni(111) Interface, *Applied Physics Letters* **96**, 012504 (2010).
  - [9] J. C. Leutenantsmeyer, A. A. Kaverzin, M. Wojtaszek, and B. J. van Wees, Proximity Induced Room Temperature Ferromagnetism in Graphene Probed with Spin Currents, *2D Materials* **4**, 014001 (2016).
  - [10] Z. Wang, C. Tang, R. Sachs, Y. Barlas, and J. Shi, Proximity-Induced Ferromagnetism in Graphene Revealed by the Anomalous Hall Effect, *Physical Review Letters* **114**, 016603 (2015).
  - [11] H. Haugen, D. Huertas-Hernando, and A. Brataas, Spin Transport in Proximity-induced Ferromagnetic Graphene, *Physical Review B* **77**, 115406 (2008).
  - [12] D. V. Tuan and S. Roche, Spin Manipulation in Graphene by Chemically Induced Pseudospin Polarization, *Physical Review Letters* **116**, 106601 (2016).
  - [13] Y. Dedkov and E. Voloshina, Graphene Growth and Properties on Metal Substrates, *Journal of Physics: Condensed Matter* **27**, 303002 (2015).
  - [14] V. Fal'ko, Quantum Information on Chicken Wire, *Nature Physics* **3**, 151 (2007).
  - [15] Y. S. Dedkov and M. Fonin, Electronic and Magnetic Properties of the Graphene–ferromagnet Interface, *New Journal of Physics* **12**, 125004 (2010).
  - [16] A. Dahal and M. Batzill, Graphene–nickel interfaces: a review, *Nanoscale* **6**, 2548 (2014).
  - [17] E. Voloshina and Y. Dedkov, Electronic and Magnetic Properties of the Graphene- Ferromagnet Interfaces: Theory vs. Experiment, in *Physics and Applications of Graphene - Experiments*, Vol. 499 (InTech, 2011) pp. 75–78.
  - [18] E. N. Voloshina and Y. S. Dedkov, General Approach to the Understanding the Electronic Structure of Graphene on Metals, *Materials Research Express* **1**, 035603 (2014).
  - [19] J. C. W. Swart, E. van Steen, I. M. Ciobica, and R. A. van Santen, Interaction of Graphene with FCC-Co(111), *Physical Chemistry Chemical Physics* **11**, 803 (2009).
  - [20] V. M. Karpan, P. A. Khomyakov, A. A. Starikov, G. Giovannetti, M. Zwierzycki, M. Talanana, G. Brocks, J. van den Brink, and P. J. Kelly, Theoretical Prediction of Perfect Spin Filtering

- at Interfaces Between Close-packed Surfaces of Ni or Co and Graphite or Graphene, *Physical Review B* **78**, 195419 (2008).
- [21] L. L. Patera, C. Africh, R. S. Weatherup, R. Blume, S. Bhardwaj, C. Castellarin-Cudia, A. Knop-Gericke, R. Schloegl, G. Comelli, S. Hofmann, and C. Cepek, In Situ Observations of the Atomistic Mechanisms of Ni Catalyzed Low Temperature Graphene Growth, *ACS nano* , 7901 (2013).
- [22] H.-C. Mertins, S. Valencia, W. Gudat, P. M. Oppeneer, O. Zaharko, and H. Grimmer, Direct Observation of Local Ferromagnetism on Carbon in C/Fe Multilayers, *Europhysics Letters (EPL)* **66**, 743 (2004).
- [23] O. Céspedes, M. S. Ferreira, S. Sanvito, M. Kociak, and J. M. D. Coey, Contact Induced Magnetism in Carbon Nanotubes, *Journal of Physics: Condensed Matter* **16**, L155 (2004).
- [24] A. Allard and L. Wirtz, Graphene on Metallic Substrates: Suppression of the Kohn Anomalies in the Phonon Dispersion, *Nano Letters* **10**, 4335 (2010).
- [25] L. M. Malard, M. A. Pimenta, G. Dresselhaus, and M. S. Dresselhaus, Raman Spectroscopy in Graphene, *Physics Reports* **473**, 51 (2009).
- [26] I. Shlimak, A. Haran, E. Zion, T. Havdala, Y. Kaganovskii, A. V. Butenko, L. Wolfson, V. Richter, D. Naveh, A. Sharoni, E. Kogan, and M. Kaveh, Raman Scattering and Electrical Resistance of Highly Disordered Graphene, *Physical Review B* **91**, 045414 (2015).
- [27] A. C. Ferrari and D. M. Basko, Raman Spectroscopy as a Versatile Tool for Studying the Properties of Graphene, *Nature Nanotechnology* **8**, 235 (2013).
- [28] A. Reina, H. Son, L. Jiao, B. Fan, M. S. Dresselhaus, Z. Liu, and J. Kong, Transferring and Identification of Single- and Few-Layer Graphene on Arbitrary Substrates, *The Journal of Physical Chemistry C* **112**, 17741 (2008).
- [29] A. Cabrero-Vilatela, R. S. Weatherup, P. Braeuninger-Weimer, S. Caneva, and S. Hofmann, Towards a General Growth Model for Graphene CVD on Transition Metal Catalysts, *Nanoscale* **8**, 2149 (2016).
- [30] A. C. Ferrari, Raman spectroscopy of graphene and graphite: Disorder, electron-phonon coupling, doping and nonadiabatic effects, *Solid State Communications* **143**, 47 (2007).
- [31] S. Reichardt and L. Wirtz, Raman Spectroscopy of Graphene, in *Optical Properties of Graphene* (WORLD SCIENTIFIC, 2017) pp. 85–132.
- [32] A. C. Ferrari, J. C. Meyer, V. Scardaci, C. Casiraghi, M. Lazzeri, F. Mauri, S. Piscanec,

- D. Jiang, K. S. Novoselov, S. Roth, and A. K. Geim, Raman Spectrum of Graphene and Graphene Layers, *Physical Review Letters* **97**, 187401 (2006).
- [33] W. L. O'Brien and B. P. Tonner, Orbital and Spin Sum Rules in X-ray Magnetic Circular Dichroism, *Physical Review B* **50**, 12672 (1994).
- [34] H. Wang, C. Bryant, D. W. Randall, L. B. LaCroix, E. I. Solomon, M. LeGros, and S. P. Cramer, X-ray Magnetic Circular Dichroism Sum Rule Analysis of the Blue Copper Site in Plastocyanin. A Probe of Orbital and Spin Angular Momentum, *The Journal of Physical Chemistry B* **102**, 8347 (1998).
- [35] C. T. Chen, Y. U. Idzerda, H.-J. Lin, N. V. Smith, G. Meigs, E. Chaban, G. H. Ho, E. Pellegrin, and F. Sette, Experimental Confirmation of the X-ray Magnetic Circular Dichroism Sum Rules for Iron and Cobalt, *Physical Review Letters* **75**, 152 (1995).
- [36] Y. U. Idzerda, C. T. Chen, H. J. Lin, H. Tjeng, and G. Meigs, Application of Magnetic Circular Dichroism to Magnetic Thin-films, *Physics B* **208-209**, 746 (1995).
- [37] K. Amemiya, T. Yokoyama, Y. Yonamoto, D. Matsumura, and T. Ohta, O K-edge X-ray Magnetic Circular Dichroism of Atomic O Adsorbed on an Ultrathin Co/Cu(100) Film: Comparison with Molecular CO on Co/Cu(100), *Physical Review B* **64**, 132405 (2001).
- [38] Z. Sun, Y. Zhan, S. Shi, and M. Fahlman, Energy level Alignment and Interactive Spin Polarization at Organic/Ferromagnetic Metal Interfaces for Organic Spintronics, *Organic Electronics: physics, materials, applications* **15**, 1951 (2014).
- [39] H. Wende, A. Scherz, C. Sorg, K. Baberschke, E. K. U. Gross, H. Appel, K. Burke, J. Minár, H. Ebert, A. L. Ankudinov, and J. J. Rehr, XMCD analysis beyond standard procedures, *AIP Conference Proceedings* **882**, 78 (2007).
- [40] J. Vogel, A. Fontaine, V. Cros, and F. Petroff, Structure and magnetism of Pd in Pd/Fe multilayers studied by x-ray magnetic circular dichroism at the Pdsedges, *Physical Review B - Condensed Matter and Materials Physics* **55**, 3663 (1997).
- [41] C. Sorg, *Magnetic Properties of 3d and 4f Ferromagnets Studied by X-Ray Absorption Spectroscopy*, Ph.D. thesis, Freie Universität Berlin (2005).
- [42] D. J. Huang, H. T. Jeng, C. F. Chang, G. Y. Guo, J. Chen, W. P. Wu, S. C. Chung, S. G. Shyu, C. C. Wu, H. J. Lin, and C. T. Chen, Orbital Magnetic Moments of Oxygen and Chromium in CrO<sub>2</sub>, *Physical Review B* **66**, 174440 (2002).
- [43] J. Pelzl, R. Meckenstock, D. Spoddig, F. Schreiber, J. Pflaum, and Z. Frait, Spin-orbit-coupling

- effects on g-value and damping factor of the ferromagnetic resonance in Co and Fe films, *Journal of Physics Condensed Matter* **15** (2003).
- [44] M.-B. Martin, B. Dlubak, R. S. Weatherup, M. Piquemal-Banci, H. Yang, R. Blume, R. Schloegl, S. Collin, F. Petroff, S. Hofmann, J. Robertson, A. Anane, A. Fert, and P. Seneor, Protecting nickel with graphene spin-filtering membranes: A single layer is enough, *Applied Physics Letters* **107**, 012408 (2015).
- [45] B. Dlubak, M.-B. Martin, R. S. Weatherup, H. Yang, C. Deranlot, R. Blume, R. Schloegl, A. Fert, A. Anane, S. Hofmann, P. Seneor, and J. Robertson, Graphene-Passivated Nickel as an Oxidation- Resistant Spin Polarized Electrode, *ACS nano* **6**, 10930 (2012).
- [46] O. Eriksson, A. M. Boring, R. C. Albers, G. W. Fernando, and B. R. Cooper, Spin and Orbital Contributions to Surface Magnetism in 3d Elements, *Physical review. B, Condensed matter* **45**, 2868 (1992).
- [47] W. L. O'Brien, B. P. Tonner, G. R. Harp, and S. S. P. Parkin, Experimental Investigation of Dichroism Sum Rules for V, Cr, Mn, Fe, Co, and Ni: Influence of Diffuse Magnetism, *Journal of Applied Physics* **76**, 6462 (1994).
- [48] O. Eriksson, B. Johansson, R. C. Albers, A. M. Boring, and M. S. S. Brooks, Orbital Magnetism in Fe, Co, and Ni, *Physical Review B* **42**, 2707 (1990).
- [49] N. Menezes, V. S. Alves, E. C. Marino, L. Nascimento, L. O. Nascimento, and C. Morais Smith, Spin g -factor due to electronic interactions in graphene, *Physical Review B* **95**, 1 (2017).
- [50] R. Nakajima, J. Stöhr, and Y. U. Idzerda, Electron-yield Saturation Effects in L-edge X-ray Magnetic Circular Dichroism Spectra of Fe, Co, and Ni, *Physical Review B* **59**, 6421 (1999).
- [51] C. T. Chen, F. Sette, Y. Ma, and S. Modesti, Soft-x-ray Magnetic Circular Dichroism at the L<sub>2,3</sub> Edges of Nickel, *Physical Review B* **42**, 7262 (1990).
- [52] C. Chacon, O. Isnard, L. Chioncel, C. Giorgetti, F. Baudelet, and E. Dartyge, XMCD Measurements and Calculations at the Co K Edge in YCo<sub>4</sub>B, *Journal of Magnetism and Magnetic Materials* **242-245**, 861 (2002).
- [53] P. Söderlind, O. Eriksson, B. Johansson, R. C. Albers, and A. M. Boring, Spin and Orbital Magnetism in Fe-Co and Co-Ni Alloys, *Physical Review B* **45**, 12911 (1992).
- [54] Y. J. Song, A. F. Otte, Y. Kuk, Y. Hu, D. B. Torrance, P. N. First, W. A. De Heer, H. Min, S. Adam, M. D. Stiles, A. H. MacDonald, and J. A. Stroscio, High-resolution tunnelling

- spectroscopy of a graphene quartet, *Nature* **467**, 185 (2010).
- [55] P. V. Semenikhin, A. N. Ionov, and M. N. Nikolaeva, Electron Spin Resonance in a Multilayer Graphene Synthesized with Polystyrene, *Technical Physics Letters* **46**, 186 (2020).
- [56] M. Björck and G. Andersson, GenX: An Extensible X-ray Reflectivity Refinement Program Utilizing Differential Evolution, *Journal of Applied Crystallography* **40**, 1174 (2007).
- [57] P. A. Kienzle, J. Krycka, N. Patel, and I. Sahin, Refl1D (2016).
- [58] J. F. Ankner and C. F. Majkrzak, Subsurface Profile Refinement for Neutron Specular Reflectivity, in *Subsurface profile refinement for neutron specular reflectivity*, Vol. 1738, edited by C. F. Majkrzak and J. L. Wood (1992) pp. 260–269.
- [59] F. A. Ma’Mari, T. Moorsom, G. Teobaldi, W. Deacon, T. Prokscha, H. Luetkens, S. Lee, G. E. Sterbinsky, D. A. Arena, D. A. MacLaren, M. Flokstra, M. Ali, M. C. Wheeler, G. Burnell, B. J. Hickey, and O. Cespedes, Beating the Stoner Criterion Using Molecular Interfaces, *Nature* **524**, 69 (2015).
- [60] M. Hansen, R. P. Elliott, and F. A. Shunk, *Constitution of Binary Alloys* (McGraw-Hill, New York, 1958) p. 1305.
- [61] P. Braeuninger-Weimer, B. Brennan, A. J. Pollard, and S. Hofmann, Understanding and Controlling Cu-Catalyzed Graphene Nucleation: The Role of Impurities, Roughness, and Oxygen Scavenging, *Chemistry of Materials* **28**, 8905 (2016).
- [62] N. Srivastava, Q. Gao, M. Widom, R. M. Feenstra, S. Nie, K. F. McCarty, and I. V. Vlassiuk, Low-energy electron reflectivity of graphene on copper and other substrates, *Physical Review B - Condensed Matter and Materials Physics* **87**, 1 (2013).
- [63] S. D. Costa, A. Righi, C. Fantini, Y. Hao, C. Magnuson, L. Colombo, R. S. Ruoff, and M. A. Pimenta, Resonant Raman spectroscopy of graphene grown on copper substrates, *Solid State Communications* **152**, 1317 (2012).